Damage development on Antarctic ice shelves sensitive to climate warming

Izeboud, Maaike; Wouters, Bert; de Roda Husman, Sophie; Lhermitte, Stef

DOI
10.1038/s41558-025-02453-4

Publication date
2025

Document Version
Final published version

Published in
Nature Climate Change

nature climate change

Article

https://doi.org/10.1038/s41558-025-02453-4

Damage development on Antarctic ice shelves sensitive to climate warming

Received: 30 January 2024

Accepted: 4 September 2025

Published online: 17 October 2025

Check for updates

Maaike Izeboud[1,2] ✉, Bert Wouters[1], Sophie de Roda Husman[1] & Stef Lhermitte[1,3]

Damage features, such as rifts and crevasses, are the first signs of a weakened ice shelf and the precursor for retreat. Yet, damage changes are not widely quantified on Antarctic ice shelves, leaving future ice shelf weakening poorly understood. Here we use satellite imagery to detect both long-term (24-year) and short-term (annual, 2015–2021) Antarctic-wide damage changes, revealing a multiyear damage development cycle strongly correlated to ice shelf area changes, and a net decline in damaged area from 1997 to 2021. We establish a data-driven link between damage and ice flow characteristics, which shows that ice flow acceleration, strain rate increases and thinning lead to more damage development, in particular under high-emission climate scenarios. This sensitivity to warming suggests that without quantification of damage impacts by detailed physical models the (timing of) ice shelf retreat and Antarctic mass loss may currently be underestimated.

The potential instability of Antarctic ice shelves is a major uncertainty in current sea-level rise projections, either due to short-term collapse or long-term weakening[1,2]. Understanding the processes that affect the structural weakening, retreat and instability of ice shelves is therefore essential[3]. On an ice shelf, damaged areas, consisting of crevasses and/or rifts, are the first indicators of its weakening[4], affecting the load-bearing capacity of the ice. This weakening reduces the ice shelf's ability to buttress the grounded ice, which leads to dynamic thinning, speed-up of the ice flow and increases internal stress and strain rates[5,6]. Higher stresses and strain rates, in turn, promote additional damage development, creating a feedback loop that increasingly weakens the ice shelf and enhances ice mass loss through increased discharge[7,8]. Furthermore, damage is a precursor to ice shelf calving[4,9]. Damage can even set the stage for ice shelf disintegration when combined with external factors, such as hydrofracturing[10,11], unpinning or back-stress-triggered failure[5,12], sea ice or mélange removal[13], and changes in sea surface slope[14,15].

Despite the critical role of damage in ice shelf instability and retreat, large-scale spatiotemporal assessments of the evolving distribution of fractures in the (recent) past are scarce, and observationally constrained projections for the future are missing[3]. The scarcity of (surface) damage observations and damage change assessments is primarily caused by a lack of available methods that can be applied on large spatial and temporal scales. This has recently been remedied by the advent of machine-learning approaches (for example, refs. 10,16,17) and by improved image-processing techniques, such as the NormalisEd Radon transform Detection (NeRD) method[18]. Furthermore, although progress has been made, damage processes remain difficult to integrate into realistic ice sheet models, and are limited to the study of idealized scenarios[19,20]. As a result of these model limitations, the impact of damage on ice shelf stability and mass loss remains to be quantified, and there are so far no projections of damage development and damage-induced structural weakening of ice shelves for future emission scenarios.

To advance our understanding of ice shelf dynamics and improve the projected contribution of Antarctica to sea-level rise, it is crucial that we assess the effect of climate change on damage-induced weakening and retreat of ice shelves, which can potentially lead to instability and collapse. In this study, we present a multidecadal analysis of damage changes on ice shelves across Antarctica, complementing existing short-term fracture density change products of refs. 16,17, and we introduce estimates of the sensitivity of damage development to different future emission scenarios.

[1]Department of Geoscience and Remote Sensing, Delft University of Technology, Delft, Netherlands. [2]Department of Water and Climate, Vrije Universiteit Brussel, Brussels, Belgium. [3]Department of Earth & Environmental Sciences, KU Leuven, Leuven, Belgium. ✉e-mail: maaike.izeboud@vub.be

https://doi.org/10.1038/s41558-025-02453-4

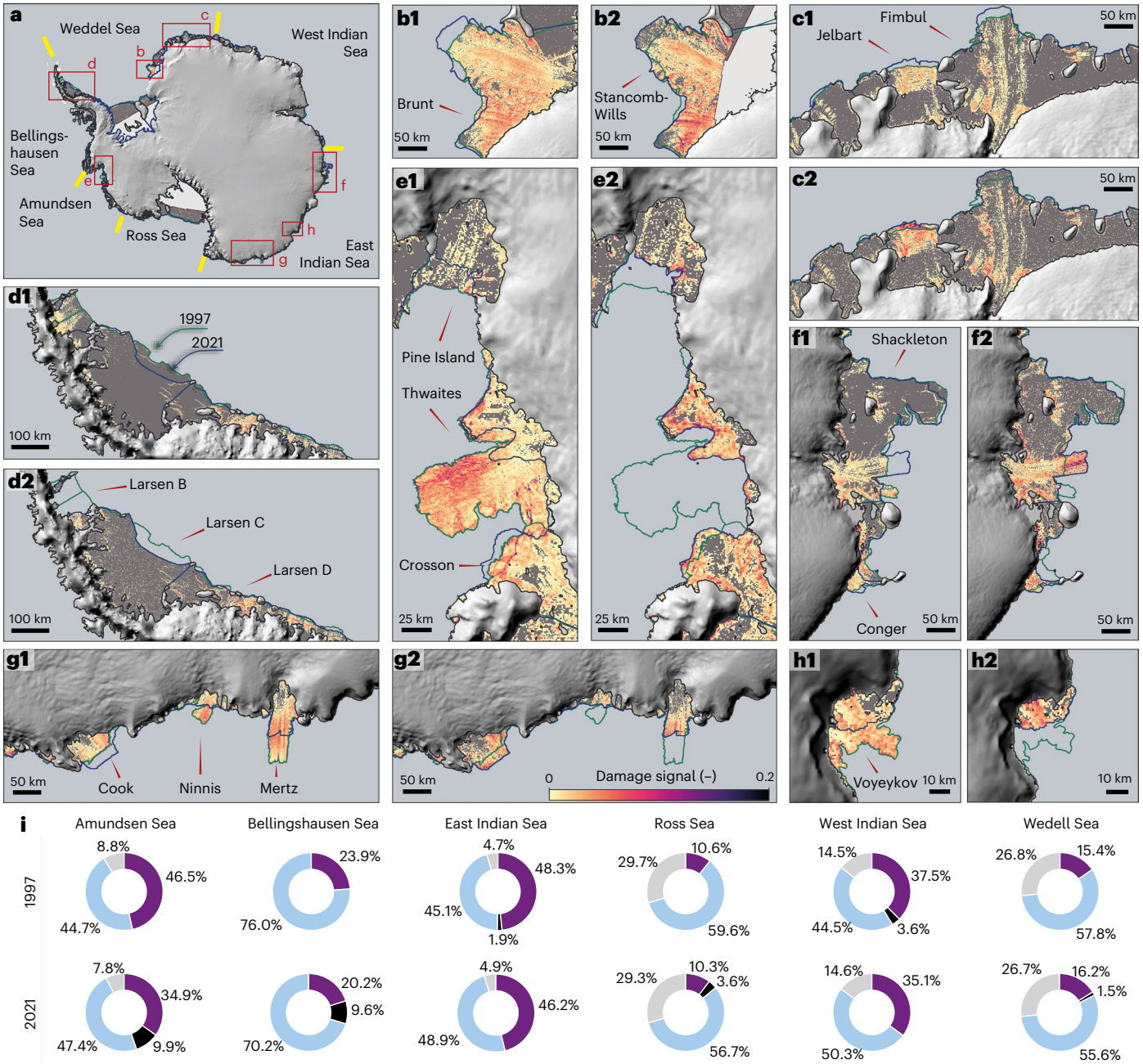

Fig. 1 | Long-term damage change between 1997 and 2021. a, Pan-Antarctic damage in 2021 with sector boundaries used for aggregation (yellow lines) and zoom boxes for panels **b**–**h**. **b**–**h**, Observed damage signal for selected ice shelves in 1997 (**b1**–**h1**; left) and 2021 (**b2**–**h2**; right): **b**, Brunt, **c**, Jelbart and Fimbul, **d**, Larsen A-D, **e** Pine Island, Thwaites and Crosson, **f**, Shackleton and Conger, **g**, Cook, Ninnis and Mertz and **h**, Voyeykov ice shelves. Ice shelf fronts shown in pink (1997) and blue (2021) (adapted from ref. 31); grounding line in black[32]; background is shaded Antarctic DEM[33]. **i**, Pie charts showing damaged area (purple), non-damaged area (light blue), and no data (light grey) per sector. A black wedge indicates area change between 1997 and 2021 (for example, the calved area of the Amundsen Sea sector displayed in 2021). Basemaps in **a**–**h** from ref. 33 under a Creative Commons licence CC BY. Grounding line shapefiles in **a**–**h** from ref. 32 under a Creative Commons licence CC BY. Ice-front shapefiles in **a**–**h** from ref. 31 under a Creative Commons license CC BY.

Observations of damage change

To assess Antarctic-wide damage states, we used the NeRD method, which is applicable to satellite data at varying spatial resolutions[18], and therefore uniquely suited to generate assessments that span different satellite missions. We apply NeRD to both the RADARSAT RAMP mosaics of 1997 and 2000 (100-m resolution) and Sentinel-1 Synthetic Aperture Radar images (40-m resolution) acquired between 2015 and 2021, and thereby construct the first extensive multidecadal (24-year) time series depicting the evolution of damage at the ice shelf surface (Fig. 1 and Extended Data Fig. 1). Sensor-induced differences were accounted for and minimized (Methods). By using the NeRD method, we detect features at the ice shelf surface only—all visible crevasses, fractures and rifts—and group these under the umbrella term 'damage' or 'damaged area', distinguishing these from the damage parameter commonly used in continuum mechanics literature[19,20] and not including basal fractures. With the detected damage we study the effects of damage on the strength of the ice (structural stability or weakening) rather than on the rheology of ice.

Our observations reveal a noteworthy 7.8% Antarctic-wide decline in damaged ice shelf area of 13,200 km^2 from 1997 to 2021. The general

https://doi.org/10.1038/s41558-025-02453-4

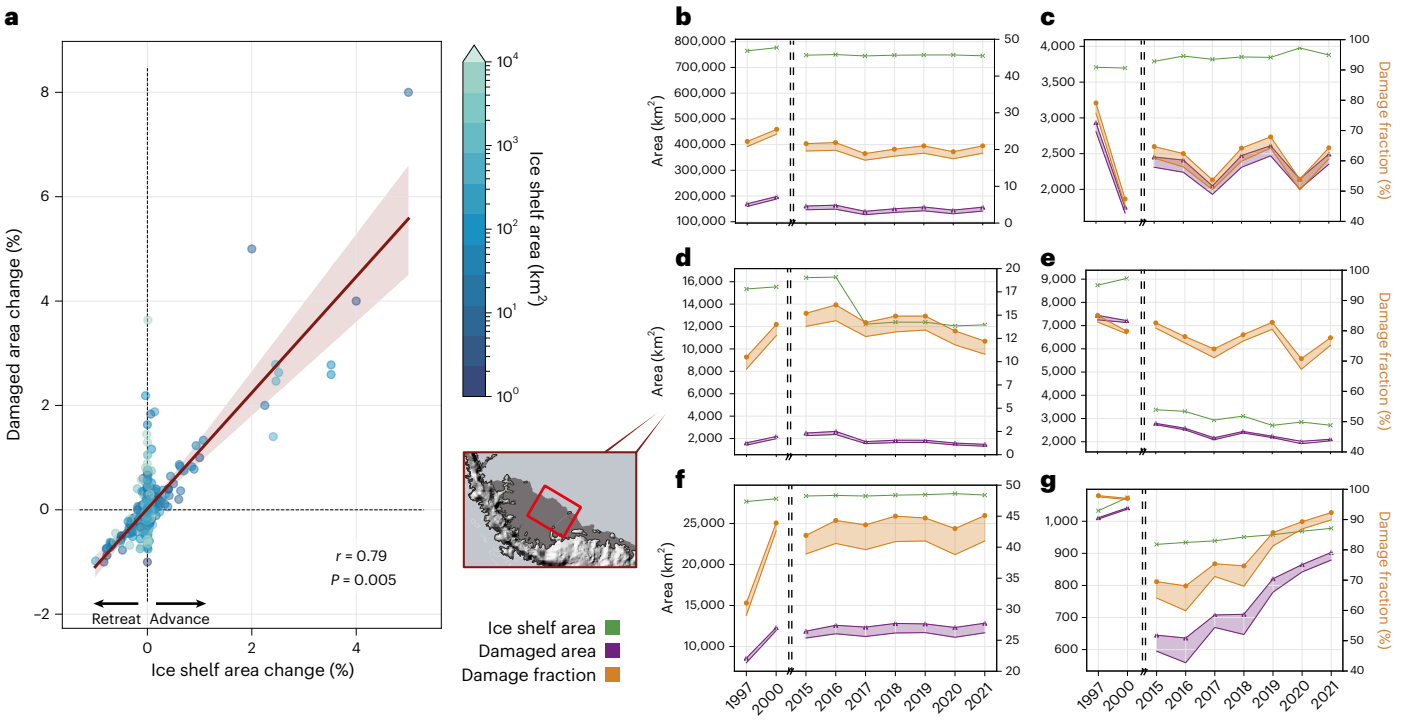

Fig. 2 | Relationship between damaged area changes and ice shelf area changes (advance/retreat). a, Correlation between damaged and total area changes (%) for all ice shelves from 1997, 2000 and annually from 2015 to 2021. Colours indicate ice shelf size. **b**,**c**–**g**, Time series for pan-Antarctic (**b**) and the Crosson (**c**), Larsen C-A68 (**d**), Thwaites (**e**), Shackleton (**f**) and Drygalski (**g**) ice shelves showing annual damaged (purple) and ice shelf (green) area (left *y* axis) and the fraction of damaged area (orange, right *y* axis). Shaded area shows uncertainty from stricter damage assessment (Methods). Note the different *y* axis for damage fraction between the panels. The data in **d** show the changes for the red area defined in the inset on the Larsen C Ice Shelf. Inset basemap from ref. 33 under a Creative Commons licence CC BY.

decline in damaged area is evident in four out of six defined sectors (Fig. 1), with the most significant reductions observed in the Amundsen Sea Embayment and Bellingshausen Sea Embayment sectors, experiencing decreases of 1,440 km² (39.0% area reduction) and 500 km² (33.2%), respectively. Whereas 46.5% of the total ice shelf area in the Amundsen Sea Embayment was damaged in 1997, this reduced to 34.0% in 2021 (Fig. 1i). The decrease in the damaged ice shelf area occurs together with an Antarctic-wide decrease in the overall ice shelf area by 19,200 km² (2.5% area reduction). At the Amundsen and Bellingshausen Sea Embayment sectors, the losses of ice shelf area are 1,200 km² (19.0%) and 830 km² (10.8%), respectively. In contrast, the Weddell Sea and East Indian Sea sectors display a respective 3.6% and 4.5% increase in damaged area, while the ice shelf area decreased by 1.8% and 2.3%, respectively.

These findings show that specifically the highly damaged areas on ice shelves have calved, given that the relative reduction in damaged area surpasses the relative reduction in the overall ice shelf area. This confirms that damage acts as a precursor to calving[12,13], in line with the findings of Pang et al.[16]. Between 2004 and 2014, they reported a ~4% reduction of pan-Antarctic surface fracture extent, attributing it to surface fracture loss within 20 km of the ice front.

The panels in Fig. 1 provide examples of heavily damaged areas in 1997 that have calved by 2021, such as the Thwaites Ice Tongue (Fig. 1e) and the Mertz, Ninnis and Voyeykov ice shelves (Fig. 1g,h). In contrast, we also identify a few ice shelves, such as Jelbart, Shackleton and Cook (Fig. 1c,f,g), that exhibit area expansion alongside an increase in damaged area, indicating a potential for upcoming calving events. Lastly, we highlight a few ice shelves with limited changes in damage patterns despite ice shelf area increases (until 2021), such as Brunt–Stancomb and Fimbul (Fig. 1b,c).

Damage development and ice shelf retreat

Because long-term surface damage change (Fig. 1) suggests that highly damaged areas are removed during calving events, we validate this relationship using short-term observations by generating annual surface damage change assessments. These are calculated as the difference between two adjacent years from 2015 to 2021, based on Sentinel-1 data covering all ice shelves (Extended Data Figs. 1–3). The annual satellite observations of changes in damaged area reveal a strong positive correlation ($r = 0.79$, $P < 0.01$) with annual changes in total ice shelf area (Fig. 2a). This underscores the cyclic nature of damage development on ice shelves (illustrated in Fig. 3a,b): damage accumulates and eventually leads to calving (area reduction), which removes the damaged areas. Subsequently, the remaining ice shelf gradually advances and accrues new damage. Figure 2a also displays a number of instances with area changes close to 0% while damage increases, indicating the relative weakening of these ice shelves.

While the long-term assessment reveals a total loss of damaged area between 1997 and 2021, the annual assessments unveil fluctuations throughout the years. Antarctic-wide fluctuations are relatively small (Fig. 2b), and occur on a timescale of only a few years. The fraction of damaged area to ice shelf area varies between 18.9% (2017) and 21.0% (2021), suggesting a quasi-stable cycle of damage development across the continent in the past decade, and most damaged ice shelf area loss having occurred after the peak in 2000 (25.5%). A lower bound to the damage assessment is included that accounts for the remaining bias between damage values detected by the RAMP and Sentinel-1 dataset, providing an uncertainty of 1.8% in the damage fraction.

The damage development cycle is exemplified for select ice shelves in Fig. 2c–g, which show that the variations of damaged area and damage fraction for individual ice shelves can be much larger than on regional scales. On the Crosson, Larsen C and Thwaites ice shelves, both

https://doi.org/10.1038/s41558-025-02453-4

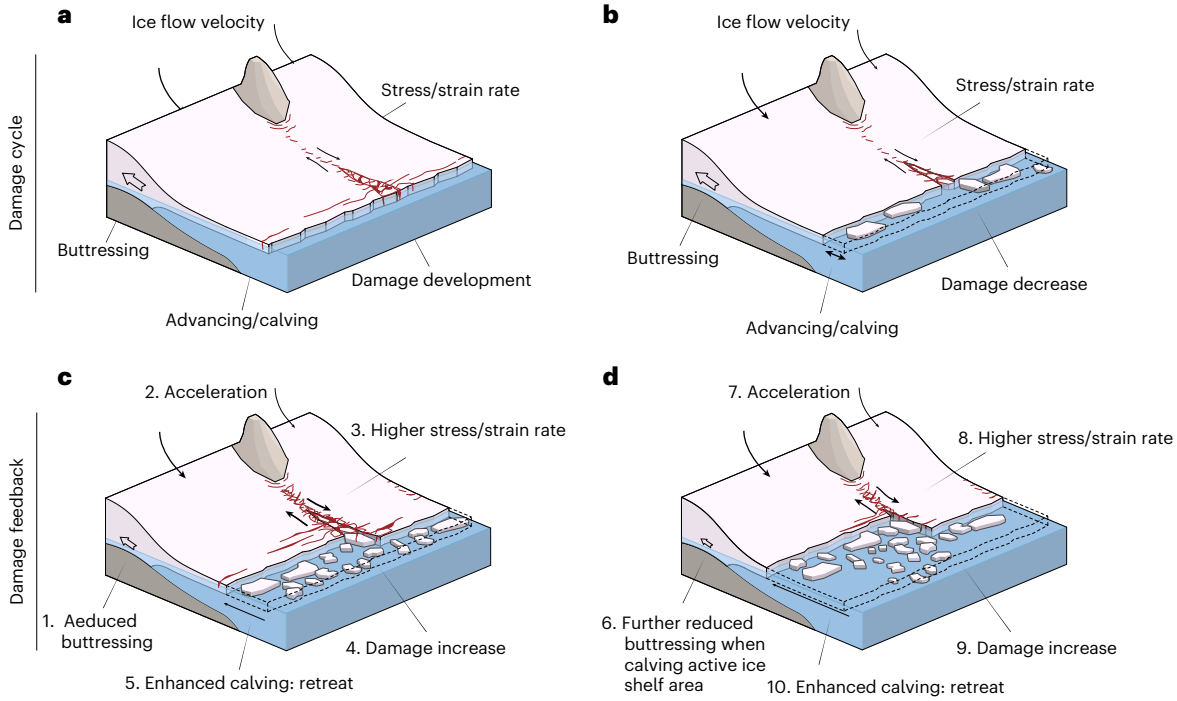

Fig. 3 | Damage impact on ice shelf weakening and retreat. a–**d**, Schematic showing ice shelf advance and retreat during a typical damage cycle (from advanced (**a**) to retreated (**b**) state) versus enhanced retreat driven by damage feedback (**c**,**d**). Ice shelf states in **a**,**b** are recurring. In **c**, once buttressing is reduced (1), a positive feedback is activated that accelerates ice flow (2), enhances internal strain rates (3) which enhances damage development (4) and calving (5). This further reduces buttressing and continues retreat (**d**, number 6 onwards) with no (or very slow) recovery to the original extent. Credit: illustrations, Iris van der Heide.

the damaged area and damage fraction exhibit fluctuations through the years. Noteworthy calving events, such as the calving of iceberg A68[21] on the Larsen C ice shelf in July 2017 are preceded by an increase in damaged area and damage fraction (that is, ice shelf structural weakening) before the event, followed by a decrease in both after the event. Additionally, ice shelves such as Drygalski and Shackleton exhibit a consistent expansion of ice shelf area and damaged area between 2015 and 2021, indicating an overall damage-induced weakening over time and a heightened likelihood of an upcoming calving event. These examples show how specific ice shelves advance and calve in tandem with damage development, indicating how they are in a mechanically weakened state prior to calving.

Link to ice dynamics with regression model

We train a random forest regression model that is able to estimate damage values based on fundamental ice dynamic parameters, as derived from satellite observations (Methods). Similar to Emetc et al.[22], our regression model is established on key features, consisting of ice flow velocity; principal, longitudinal, transverse, shear and effective strain rate components; ice thickness; and annual changes in principal strain rate and ice flow velocity (nine features, from 2015 to 2021; Extended Data Fig. 4 and Extended Data Table 1). The evaluation of the random forest regression is detailed in Methods, and performs well in reproducing damage patterns (giving structural similarity indexes of 0.70 and 0.78 for spatial and temporal test sets, respectively), but has difficulty reproducing high damage signal values (Methods and Extended Data Fig. 5). We therefore continue our analysis focusing on relative changes (higher or lower) of the predicted damage, rather than absolute values.

The regression model learns the empirical relationship between the provided ice properties and observed damage. It shows the relative feature importance, noting ice thickness, longitudinal strain rate and ice velocity as the most important of the nine features (respective fractions, 0.19, 0.15, 0.15), although all are significant (lowest importance, 0.06). The model shows that higher values of all strain rate components, increased velocity or a decrease in ice thickness yield higher damage values (Extended Data Fig. 6).

This relationship shows that dynamic thinning and acceleration of the ice flow are highly correlated to, and potentially can cause, increased damage development. If this new damage then results in calving and loss of active ice shelf area, it leads to less buttressing and subsequent ice shelf speed-up[8,23], further enhancing damage development[7], structural weakening and retreat of the ice shelf (damage feedback, illustrated in Fig. 3c,d).

Although the damage feedback has been demonstrated in modelling studies[7,8], our results now capture the influence of ice dynamics on damage development from large-scale spatiotemporal observations. However, observed changes in ice shelf and damage extent do not suggest that this feedback has triggered runaway retreat during the study period, as we detect cyclic patterns in recent years (Fig. 2). Nevertheless, ice shelves in a structurally weakened state are more vulnerable to sudden collapse when, for example, inundated with meltwater[10] or during periods of low sea ice concentration[13].

Damage development sensitive to future climate

To generate projections of future damage development under different climate scenarios, we apply the developed regression model to the outputs of five ice sheet model projections participating in the Ice Sheet Model Intercomparison for CMIP6 (ISMIP-6) project[24], including PISM[25], SICOPOLIS[26], MALI[27], ISSM[28] and CISM[29]. These datasets provide a quantification of the key ice properties in various future climate scenarios from 2015 to 2100, and therefore offer a means to project estimates of damage into the future and assess how much damage development would vary between these scenarios. Selected for their relatively high spatial resolution (≤8 km), these models incorporate data from four different climate forcing experiments. The predicted

https://doi.org/10.1038/s41558-025-02453-4

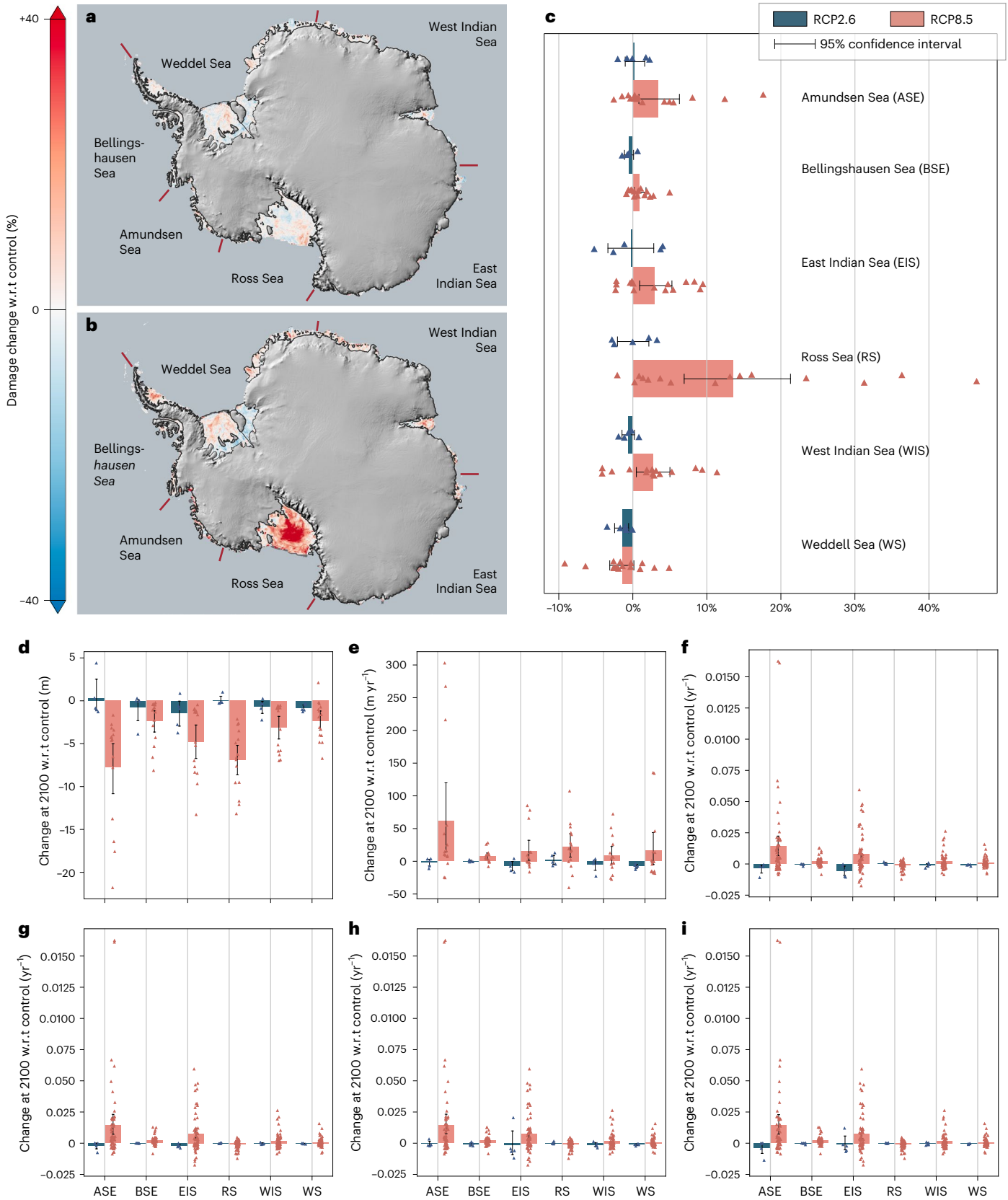

Fig. 4 | Projections of damage change (%) by 2100. a,**b**, Maps of the ensemble mean grouped for two climate-forcing pathways, RCP2.6 (**a**) and RCP8.5 (**b**). Grounded ice[32] visualized with Antarctic DEM[33]. **c**–**i**, Integrated values per sector, including data points for each model/experiment combination, for change in damage (**c**) and change in surface elevation (**d**), ice flow velocity (**e**), maximum principal strain rate (**f**), transverse strain rate (**g**), longitudinal strain rate (**h**) and shear strain rate (**i**) from ISMIP-6 models at 2100. Predicted damage values were obtained from the trained random forest regression model, with input data from five ice sheet models (PISM[25], SICOPOLIS[26], MALI[27], ISSM[28] and CISM[29]), and are calculated relative (%) to the control simulation of each model. Basemaps in **a** and **b** from ref. 33 under a Creative Commons licence CC BY. Grounding line shapefiles in **a** and **b** from ref. 32 under a Creative Commons licence CC BY.

damage values of each experiment are compared to the predictions with the control experiment, which simulates conditions representative of the recent past, to calculate the sensitivity (that is, the relative damage changes) at each time step (Extended Data Figs. 7–9). It should be noted that these experiments explore the diverse responses of ice sheet models to the Representative Concentration Pathway (RCP) scenarios rather than representing a mean pathway. Consequently, the projected damage changes should be considered as indicative of the potential range (sensitivity and sign) of responses compared with a control run that uses present-day conditions, rather than as a single predicted trajectory.

Our ensemble mean projections, depicted in Fig. 4, highlight the sensitivity of damage to future emission scenarios. Figure 4a indicates a slight decrease in damage for low-emission scenarios associated with RCP2.6 of −0.8% (−2.9% to 0.7% model range) across the Antarctic domain by 2100, compared to the control simulations. Conversely, for the high-emission pathway RCP8.5, we project an increase in damage by 3.2% (−5% to 14% model range, Fig. 4b,c). This projected increase in damage under RCP8.5 coincides with increased ice shelf velocity (3%, averaged over total ice shelf area), thinning (8%) and increased strain rates (~120–770% depending on the component, Fig. 4d–i), reinforcing the notion of a general damage-induced structural weakening of the ice shelves with respect to the control simulation.

Distinct regional variations are observed (Fig. 4c), with the Amundsen Sea, West Indian, East Indian and Ross Sea sectors exhibiting a very strong sensitivity of damage development to different climate forcing scenarios. These sectors yield increased damage development for RCP8.5, which results from a combination of ice flow acceleration, ice shelf thinning and increased strain rates (Fig. 4d–i). For example, strong increases in damage are predicted at the centre of the Ross Ice Shelf in the RCP8.5 scenario primarily due to thinning and increased shear strain rates resulting from localized ice shelf acceleration and deceleration near the ice front. This insinuates that, if the velocity gradient between ice streaming in from Ross-West and Ross-East ice shelves increases, the centre of the Ross Ice Shelf might start behaving more similarly to a shear zone as we see at Pine Island Glacier, with increased damage development as a result. However, this would be a rather extreme change in behaviour, and requires further investigation with process-based models. In contrast, the Weddell Sea and Bellingshausen Sea sectors display a less sensitive damage development regime, demonstrating fewer differences between a low or high climate-forcing scenario.

Discussion

This study provides perspective on continent-wide changes in damaged areas across Antarctic ice shelves over an extended 24-year period from 1997 to 2021, with annual observations from 2015 to 2021. Our observations reveal a long-term reduction of damage on Antarctic ice shelves attributed to the calving of compromised ice shelf regions. Notably, a strong correlation between damaged area changes and ice shelf area changes over the last seven years underscores the link between damage-induced structural weakening and subsequent calving and ice shelf retreat. Increases in damaged area and damage fraction prior to calving suggest that ice shelves are in a weakened state before calving occurs.

This study introduces estimates of how future damage development would be affected by different climate scenarios, by empirically linking observed damage to key ice shelf parameters. Our projections highlight the sensitivity of future damage development to emission pathways in multiple sectors. Under high-emission scenarios, we anticipate intensified damage development, particularly in regions where ice shelves thin and accelerate (driven by increased ocean melt[30]), coupled with substantial increases in strain rates. This underscores the intricate interplay between weakened ice shelves, accelerated flow and damage development with notable vulnerabilities predicted in the Amundsen, East Indian and Ross Sea sectors. Although this is consistent with observed structural weakening in the Amundsen Sea sector (this manuscript, refs. 5,8), the Ross Sea sector currently shows relatively low levels of weakening. The projected high sensitivity to future climate warming underscores the importance of improving our understanding and representation of damage processes in ice sheet models to assess whether Ross could shift to a more vulnerable regime.

The implications of observed and predicted sensitivity of damage development on ice shelves with respect to Antarctic mass loss are twofold. First, our findings suggest that highly damaged ice shelves are more likely to calve, making them more susceptible to significant retreat or collapse due to external forcing[10–15]. Second, we establish that damage—and thereby structural weakening of ice shelves—increases with acceleration and thinning, showing how a loss of buttressing with subsequent ice shelf speed-up can lead to enhanced damage development. These two impacts compound when damage leads to calving of buttressing ice shelf areas, eventually leading to more damage development (damage feedback) and increasing mass loss. The strength of this feedback, and whether it could lead to runaway retreat, could not be quantified here.

In conclusion, our study underscores the importance of including damage impacts in ice sheet models and future mass loss assessments. Our projections indicate that damage is sensitive to the trajectory of future climate scenarios and is likely to increase in a warmer climate, with consequences for ice shelf stability. Without quantification of damage impacts on mass loss by process-based model studies the (the timing of) ice shelf retreat and Antarctic mass loss may currently be underestimated. Addressing this underestimation is vital for improving the representation of ice shelf stability and refining our understanding of Antarctica's contribution to sea-level rise.

Online content

Any methods, additional references, Nature Portfolio reporting summaries, source data, extended data, supplementary information, acknowledgements, peer review information; details of author contributions and competing interests; and statements of data and code availability are available at https://doi.org/10.1038/s41558-025-02453-4.

References

1. Fox-Kemper, B. et al. in *Climate Change 2021: The Physical Science Basis. Contribution of Working Group I to the Sixth Assessment Report of the Intergovernmental Panel on Climate Change* (eds Masson-Delmotte, V. et al.) 1211–1362 (Cambridge Univ. Press, 2021).
2. Robel, A. A., Seroussi, H. & Roe, G. H. Marine ice sheet instability amplifies and skews uncertainty in projections of future sea-level rise. *Proc. Natl Acad. Sci. USA* **116**, 14887–14892 (2019).
3. Bassis, J. N. et al. Stability of ice shelves and ice cliffs in a changing climate. *Annu. Rev. Earth Planet. Sci.* https://doi.org/10.1146/annurev-earth-040522-122817 (2023).
4. Borstad, C. P. et al. A damage mechanics assessment of the larsen b ice shelf prior to collapse: toward a physically-based calving law. *Geophys. Res. Lett.* **39**, L18502 (2012).
5. Miles, B. W. J. et al. Intermittent structural weakening and acceleration of the Thwaites glacier tongue between 2000 and 2018. *J. Glaciol.* **66**, 485–495 (2021).
6. Gudmundsson, G. H., Paolo, F. S., Adusumilli, S. & Fricker, H. A. Instantaneous Antarctic ice sheet mass loss driven by thinning ice shelves. *Geophys. Res. Lett.* **46**, 13903–13909 (2019).
7. Lhermitte, S. et al. Damage accelerates ice shelf instability and mass loss in amundsen sea embayment. *Proc. Natl Acad. Sci. USA.* **117**, 24735–24741 (2020).
8. Surawy-Stepney, T., Hogg, A. E., Cornford, S. L. & Davison, B. J. Episodic dynamic change linked to damage on the thwaites glacier ice tongue. *Nat. Geosci.* **16**, 37–43 (2023).

9. Rydt, J. D., Gudmundsson, G. H., Nagler, T. & Wuite, J. Calving cycle of the Brunt Ice Shelf, Antarctica, driven by changes in ice shelf geometry. *Cryosphere* **13**, 2771–2787 (2019).
10. Lai, C. Y. et al. Vulnerability of Antarctica's ice shelves to meltwater-driven fracture. *Nature* **584**, 574–578 (2020).
11. Robel, A. A. & Banwell, A. F. A speed limit on ice shelf collapse through hydrofracture. *Geophys. Res. Lett.* **46**, 12092–12100 (2019).
12. Benn, D. I. et al. Rapid fragmentation of Thwaites eastern ice shelf. *Cryosphere* **16**, 2545–2564 (2022).
13. Arthur, J. F. et al. The triggers of the disaggregation of Voyeykov Ice Shelf (2007), Wilkes Land, East Antarctica, and its subsequent evolution. *J. Glaciol.* https://doi.org/10.1017/jog.2021.45 (2021).
14. Christie, F. D. W. et al. Antarctic ice-shelf advance driven by anomalous atmospheric and sea-ice circulation. *Nat. Geosci.* **15**, 356–362 (2022).
15. Massom, R. A. et al. Antarctic ice shelf disintegration triggered by sea ice loss and ocean swell. *Nature* **558**, 383–389 (2018).
16. Pang, A. et al. The distribution and evolution of surface fractures on pan-Antarctic ice shelves. *Int. J. Digit. Earth* **16**, 3295–3320 (2023).
17. Surawy-Stepney, T., Hogg, A. E., Cornford, S. L. & Hogg, D. C. Mapping Antarctic crevasses and their evolution with deep learning applied to satellite radar imagery. *Cryosphere* **17**, 4421–4445 (2023).
18. Izeboud, M. & Lhermitte, S. Damage detection on antarctic ice shelves using the normalised radon transform. *Remote Sens. Environ.* https://doi.org/10.1016/j.rse.2022.113359 (2023).
19. Kachuck, S. B., Whitcomb, M., Bassis, J. N., Martin, D. F. & Price, S. F. Simulating ice-shelf extent using damage mechanics. *J. Glaciol.* https://doi.org/10.1017/jog.2022.12 (2022).
20. Sun, S., Cornford, S. L., Moore, J. C., Gladstone, R. & Zhao, L. Ice shelf fracture parameterization in an ice sheet model. *Cryosphere* **11**, 2543–2554 (2017).
21. Larour, E., Rignot, E., Poinelli, M. & Scheuchl, B. Physical processes controlling the rifting of Larsen C Ice Shelf, Antarctica, prior to the calving of iceberg A68. *Proc. Natl Acad. Sci. USA* **118**, e2105080118 (2021).
22. Emetc, V., Tregoning, P., Morlighem, M., Borstad, C. & Sambridge, M. A statistical fracture model for antarctic ice shelves and glaciers. *Cryosphere* **12**, 3187–3213 (2018).
23. Fürst, J. J. et al. The safety band of Antarctic ice shelves. *Nat. Clim. Change* **6**, 479–482 (2016).
24. Seroussi, H. et al. ISMIP6 Antarctica: a multi-model ensemble of the Antarctic ice sheet evolution over the 21st century. *Cryosphere* **14**, 3033–3070 (2020).
25. Winkelmann, R. et al. The Potsdam Parallel Ice sheet Model (PISM-PIK)—part 1: model description. *Cryosphere* **5**, 715–726 (2011).
26. Greve, R. et al. ISMIP6 future projections for the Antarctic ice sheet with the model SICOPOLIS. *Zenodo* https://doi.org/10.5281/zenodo.4035932 (2020).
27. Hoffman, M. J. et al. MPAS-Albany Land Ice (MALI): a variable-resolution ice sheet model for earth system modeling using Voronoi grids. *Geosci. Model Dev* **11**, 3747–3780 (2018).
28. Schlegel, N.-J. et al. Exploration of Antarctic ice sheet 100-year contribution to sea level rise and associated model uncertainties using the ISSM framework. *Cryosphere* **12**, 3511–3534 (2018).
29. Lipscomb, W. H. et al. ISMIP6-based projections of ocean-forced Antarctic ice sheet evolution using the Community Ice Sheet Model. *Cryosphere* **15**, 633–661 (2021).
30. Naughten, K. A., Holland, P. R. & Rydt, J. D. Unavoidable future increase in west Antarctic ice-shelf melting over the twenty-first century. *Nat. Clim. Change* **13**, 1222–1228 (2023).
31. Greene, C. A., Gardner, A. S., Schlegel, N. J. & Fraser, A. D. Antarctic calving loss rivals ice-shelf thinning. *Nature* **609**, 948–953 (2022).
32. Mouginot, J., Scheuchl, B. & Rignot, E. Measures Antarctic boundaries for ipy 2007–2009 from satellite radar, version 2. NASA National Snow and Ice Data Center Distributed Active Archive Center https://nsidc.org/data/nsidc-0709/versions/2 (2017).
33. Liu, H., Jezek, K. C., Li, B. & Zhao, Z. Radarsat Antarctic Mapping Project Digital Elevation Model (NSIDC-0082, Version 2). NASA National Snow and Ice Data Center Distributed Active Archive Center https://doi.org/10.5067/8JKNEW6BFRVD (2015).

Methods

Data for damage detection

We employ data from two distinct sources to create damage maps on Antarctic ice shelves: the image mosaics of the Radarsat-1 Antarctic Mapping Project (RAMP) of 1997 and 2000 (ref. 34) and Sentinel-1 Synthetic Aperture Radar (SAR) images for the years 2015–2021.

The RAMP Mosaics are composed of SAR observations obtained by the Antarctic Mapping Mission 1 (AMM-1) and Modified Antarctic Mapping Mission (MAMM) acquired between September and November 1997 and 2000, respectively. Radarsat-1 functioned at a C-band frequency of 5.3 GHz (ref. 34). The mosaics were constructed using HH polarization at a spatial resolution of 100 m. We only processed data covering Antarctic ice shelves.

For the period 2015–2021, we obtained Sentinel-1 SAR Ground Range Detected images, focusing on overpasses occurring in September–November to mirror the RAMP acquisition season. We used the HH polarization band with a C-band frequency of 5.4 GHz, selecting ascending-orbit images in Extra Wide (EW) swath mode, with 40-m resolution. We did not apply speckle filtering, as a noise removal step is included in the NeRD method. To reduce data volume while keeping maximum spatial coverage, we used the first acquisition from each unique relative orbit (property 'relativeOrbitNumber_start') each year. This yielded between 123 and 212 images per year, totalling 1,638 processed Sentinel-1 images. Sentinel-1 images were acquired through the Google Earth Engine (GEE)[35], with code and full image list provided in the manuscript repository[36].

The Sentinel-1 EW data coverage over Antarctica is constrained to coastal areas[37], resulting in data gaps over inland sections of the Amery, Filchner–Ronne and Ross ice shelves (Extended Data Fig. 1). To maintain consistency in our spatially aggregated values, we have masked these no-data areas from the RAMP dataset as well (Extended Data Fig. 2). Furthermore, regions with inconsistent annual coverage (for example, part of the Getz Ice Shelf and a few ice shelves in Wilkes Land) were also masked for the computation of all annual spatially aggregated values, but not from the shown annual damage maps in Extended Data Fig. 2.

We used the MEaSUREs[32] grounding line to remove grounded areas and kept this static over the study period. Annual ice-front positions from ref. 31 were manually adjusted to match the ice fronts in our Sentinel-1 dataset (obtained half a year later for each year than the data used by ref. 31) and remove ocean areas. An example of the ice-front positions is included in Extended Data Fig. 1c.

Damage detection method

We employed the NeRD detection method[18]. NeRD is a line-detection algorithm suited for processing multisource remote-sensing imagery at varying spatial resolutions, enabling consistent processing of both RAMP and Sentinel-1 datasets. NeRD detects diverse morphological damage expressions, including surface crevasses, large rifts and chaotic fracture zones. NeRD computes a continuous damage signal based on the greyscale contrast of linear features within small $N \times N$ pixel kernels of the (satellite) image. Each kernel yields a single damage signal value ($\hat{D}$) within the range of 0–0.5 (unit-less).

To ensure consistency in resolution for our long-term damaged area change assessment, RAMP and Sentinel-1 images were processed with NeRD using different kernel sizes. The RAMP mosaics with 100-m resolution were processed with 10 × 10 pixel kernels (no overlap) and the Sentinel-1 data of 40-m resolution with 25 × 25 pixel kernels, such that both yield damage maps of 1,000-m resolution.

NeRD accounts for differences between sensors using a sensor- and resolution-specific noise-filtering step. For each sensor/resolution combination, we calculated a noise threshold (τ) following ref. 18, defined as the 95th percentile NeRD signal over an undamaged area (manually defined). The specific threshold values are: $\tau_{\mathrm{RAMP;100m:10px}} = 0.016$; $\tau_{\mathrm{S1;40m:25px}} = 0.041$; $\tau_{\mathrm{S1;100m:10px}} = 0.038$. The noise threshold is subtracted from the raw NeRD signal to remove sensor- and resolution-related biases, ensuring consistent damage assessment across datasets.

While NeRD's noise threshold minimizes discrepancies between sensors, some variations may persist due to two key factors[18]. (1) Changes in surface conditions affecting SAR backscatter, such as snow cover, surface roughness and liquid water content. We minimized these effects by acquiring all Sentinel-1 and RAMP images during the same austral fall period (September–November), and by processing multiple Sentinel-1 images for one damage map. (2) Different sensor sensitivity to spatial variability of surface conditions due to variations in look-angle, wavelength and native resolution—this may result in varying image contrasts and thus varying damage signal values for the same feature (sensor bias).

To assess this sensor bias, we tested the differences between RAMP and Sentinel-1 outputs on similar features for different processing kernel sizes for Sentinel-1. We selected a grounded ice area with strong terrain shadows (that is, feature contrast), assuming similar surface conditions in 1997 and 2021 at this location. Although NeRD signals in this region do not represent true damage, they help assess the sensor bias. We used two approaches to match RAMP's 1,000-m output resolution with Sentinel-1 data: (1) processing 40-m resolution images with a 25-pixel kernel and (2) first down-scaling 40-m to 100-m resolution images (using nearest-neighbour), then processing with a 10-pixel kernel. Results were compared to output from RAMP (100-m resolution processed with 10-pixel kernels). The average signal and standard deviation in the selected grounded area were:

$$\overline{\hat{D}_{\mathrm{RAMP;100m:10px}}} = 0.008 \pm 0.015,$$

$$\overline{\hat{D}_{\mathrm{S1;100m:10px}}} = 0.010 \pm 0.023,$$

$$\overline{\hat{D}_{\mathrm{S1;40m:25px}}} = 0.009 \pm 0.022.$$

The sensor bias is then 0.001 or 0.002, an order of magnitude smaller than the signal's standard deviation, confirming the comparability of RAMP and Sentinel-1 damage assessments.

Damage assessments obtained from overlapping Sentinel-1 images were consolidated into a single damage map per year by determining the median damage signal at overlapping pixels (Extended Data Fig. 2). The number of overlapping images varied regionally, ranging from 1 to 12–25 images, depending on the year, with a median of four overlapping images used for each pixel.

The damage maps were clipped to ice shelf areas, to remove outcrops and steeply sloped terrains prone to false feature detection. NeRD detects features by image contrast and cannot distinguish ice fractures from other high-contrast features such as rock outcrops, terrain shadows or sea ice edges. Some false feature detection might persist, for instance, where basal melt channels create surface depressions detectable by NeRD[38], although these typically produce weaker signals[18].

NeRD returns a single value per processing kernel, rather than resolving fracture shapes or crevasse opening. Spatially integrated values of damage and damage change were therefore based on the detected damaged area, calculated from a binary classification of the damage signal per 1 × 1 km^2 pixel: 'damage' ($\hat{D} > 0$) or 'no damage' ($\hat{D} = 0$). Pixel counts for both categories were summed per ice shelf using the annual updated ice shelf boundaries, and further aggregated by sector[23]. Only the parts of any ice shelf that had data coverage in all years were considered in the aggregation. For studying the calving of A68[21] we integrated over a focus area (Fig. 2). As a result, the calculated damage changes reflect new or propagating features rather than the deepening of fractures. The reported damaged areas (km^2) represent the number of output pixels that contain fractures, not the explicit extent of open fractures (such as ref. 16). To estimate uncertainty in the aggregated damaged area extent we applied a stricter damage

signal threshold of 0.001 (based on the estimated sensor bias), removing pixels with very low signals. This provides a conservative lower bound to the reported extent.

Data for random forest regression

We used random forest regression to examine the relationship between our (continuous) damage signal and key features of ice dynamics. First, observational data of each feature were used to train the random forest regression model. Next, to generate estimates of future damage development under different climate scenarios, we used values of future ice properties from ice sheet model outputs of the ISMIP-6 project[24] as input for the random forest model.

Multiple features representing ice dynamics were selected as input for the random forest model. The feature selection process was guided by the parameters' relevance[22] and their consistent availability across observational datasets (for training of the RF model) and as model outputs in the ISMIP-6 experiments (for application of the RF model). The selected key features for the regression are ice thickness; ice velocity; principal, effective, transverse, longitudinal and shear strain rate components; and (annual) temporal changes in both ice velocity and strain rates.

We trained the random forest model using detected damage from Sentinel-1 data (2015–2021) as target values. Ice thickness was approximated by the REMA surface elevation mosaic at 8-m resolution[39], assuming it to be eight times the height above flotation and held constant over time. No geoid correction was applied, because without it the REMA data distribution had a better match to the ISMIP-6 model data, which is necessary for a random forest model. Velocity data (vx, vy) were obtained from the ITS_LIVE campaign at 240-m resolution (2015–2018) and 120-m resolution (2019–2021)[40]. Both velocity and REMA data were resampled to the 1-km resolution damage map using spatial averaging. Strain rate components were derived from velocity components as nominal strains and calculated at multiple length scales to accommodate both large-scale and small-scale dynamics[41] (Extended Data Table 1). Temporal velocity and strain rate changes were calculated as annual differences (from 2015 to 2021) and smoothed using a three-year trailing maximum window.

Corresponding to the observational data used for training the random forest model, we used modelled surface velocity and surface elevation data[24] from ice sheet model output and calculated strain rates correspondingly. Recognizing limitations of random forest models in extrapolating data, we clipped the ISMIP-6 model data to the min/max range of the training (that is, observational) data. However, due to the large spatial variability in the Antarctic domain represented in the training data, most ISMIP-6 values fell within range, requiring minimal clipping.

Many ice sheet models in the ISMIP-6 project have model grid resolutions exceeding 10 km—relatively low compared with the observations. Because damage often occurs in localized regions (for example, near the ice front, after a pinning point or in the shear zone[5,42]), we developed the random forest regression model at the highest feasible resolution and selected ISMIP-6 models with ≤8-km resolution near the grounding line: the Potsdam Parallel Ice Sheet Model (PISM)[25], the SImulation COde for POLythermal Ice Sheets (SICOPOLIS)[26], MPAS-Albany Land Ice (MALI) model[27], the Ice Sheet System Model (ISSM)[28] and the Community Ice Sheet Model (CISM)[29].

All ISMIP-6 model datasets were resampled to a regular 8-km grid to ensure standardized inputs for the random forest model, utilizing nearest-neighbour interpolation. The observational datasets and damage maps were downsampled to the same grid through averaging, while all pixels without detected damage (that is, $D = 0$) were treated as NaN data. These resampling and downsampling steps were executed prior to strain rate calculations. We note that the resolution of 8 km limits the capture of fine-scale processes with the random forest model.

Random forest regression model development

The choice of random forest regression was based on its capabilities in handling multidimensional, non-linear regression challenges[43], and its resilience to feature scaling differences[44,45], which is essential given the varied data distributions in our input data. To ensure robust model development, we maintained strict spatial and temporal independence between training, validation and testing datasets.

To ensure temporal independence, data from 2015 to 2018 were used for training and 2021 for testing. Data from 2019 and 2020 were excluded due to overlap in two features calculated with three-year trailing windows.

Spatial independence was a critical consideration in the development of the random forest model, given the spatial correlation between neighbouring pixels[46,47] on the same ice shelf. To address this, we grouped pixels by ice shelf, treating each ice shelf as an independent unit, and applied group k-fold cross-validation to split the data into training, validation and testing subsets while preserving a similar distribution of target data. First, we randomly split 18 of 103 ice shelves for the spatial test set (86/14%, or 36,858/6,143 pixels), including: Abbot_3, Amery, Bach, Deakin, Dibble, Mendelssohn, Moubray, Pine Island, Publications, Rennick, Ross_East, Sandford, Shackleton, Stange, Withrow, Whittle and Wordie (names conform to ref. 32). The remaining set was randomly split into five training/validation folds, each between 82/21 and 84/19 ice shelves (80/20% or 29,500/7,400 pixels).

We optimized the random forest model through a two-step hyperparameter tuning process. First, we trained the random forest model on all features and multiple strain rate length scales, using a broad hyperparameter grid. Twenty candidate models were evaluated across five data folds using random search cross-validation. The best hyperparameter combination was chosen based on lowest mean absolute error (MAE), and the random forest model was refitted for feature importance analysis. This was used to select the most relevant strain rate length-scale (1 pixel; excluding the 5; and 15-pixel scales and the minimal principal strain rate).

In the second step, we trained the random forest model with the nine selected features. A second random search cross-validation was used to narrow the hyperparameter space, followed by a full grid search cross-validation on 96 candidates (five folds, totalling 480 fits). The final model, selected for lowest MAE (0.00979), was refitted and used as the final random forest model. The resulting hyperparameters were:

- bootstrap = false (rejected: true)
- max tree depth = 10 (rejected: 20, 30, 40, none)
- max features per node = 2 (rejected: 1, 4)
- minimum samples per leaf = 2 (rejected: 1, 4)
- minimum samples per split = 5 (rejected: 2, 10)
- number of estimators = 10 (rejected: 20, 30, 40, 50, 60, 70, 80).

The resulting feature importance (Extended Data Table 1) ranges from 0.06 to 0.19 (total of 1), confirming that all nine features contribute to predictions, although not equally.

We evaluated the random forest model using three metrics: area-weighted coefficient of determination (R^2), MAE and structural similarity index measure (SSIM, used for measuring the similarity between two images), as shown in Extended Data Fig. 5. The weighted R^2 accounts for ice shelf size, giving more weight to larger ice shelves where the error variance is lower—which was important because our training data did not perfectly align in space and time. The average MAE and SSIM per ice shelf assess the random forest model skill in capturing damage patterns, with SSIM particularly informative for evaluating spatial variability.

The random forest model performed well in both spatial and temporal tests, with high SSIM values (0.77 training, 0.70 spatial test and 0.78 temporal test) showing an aptitude for identifying high- from low-damage regions. The average MAE was 0.017 (training), 0.015 (spatial test) and 0.017 (temporal test), aligning closely with the

damage signal's standard deviation ($\hat{D} = 0.028 \pm 0.011$). The consistent performance across training and testing datasets supports the model's reliability.

However, the model exhibited limitations in predicting high damage signal values, as reflected in lower R^2 scores: 0.56 (training), 0.11 (spatial test) and 0.44 (temporal test), with larger errors at high damage values (Extended Data Fig. 5c). This can be attributed to the strong imbalance in the target values, where high damage pixels are sparse. Sampling strategies (under- or oversampling) did not improve results. This suggests there is insufficient feature disparity for the random forest model to be able to distinguish 'medium' from 'high' damage values. This seems reasonable, considering that the observed damage signal represents image contrasts rather than physical ice properties, and very high damage values may not be reflected in the physical input features of the random forest model. As the model was designed to assess relative, not absolute, damage levels, its limited performance at the high end is acceptable. Its strength lies in capturing spatial and temporal variations in damage related to ice dynamics, aligning with study's goal of evaluating potential future damage development.

To understand the obtained relationship between the input features and the predicted damage by the random forest model, we conducted tests with controlled synthetic data. We varied each input parameter independently across its 5–95 percentile range within the training dataset, while all others were held semiconstant at their median values (adding small random Gaussian noise perturbations of <5% of their respective standard deviation). The results (Extended Data Fig. 6) show that the random forest model predicts higher damage for higher strain rates, velocity and velocity change, and thinner ice.

Damage change projections

The trained random forest model was applied to output from five selected ice sheet models to project future damage. Data from five ISMIP-6 forcing experiments were used to assess the sensitivity of projected damage to different climate scenarios. We selected experiments 05–08 and the control experiment because all five models provided data for these experiments. The control experiment maintained constant climatic forcing from 2015 onward, while the other experiments introduced variations in atmospheric and oceanic conditions (see refs. 24,48).

The random forest model was run on each ice sheet model–experiment combination, and damage changes was calculated relative to each model's control experiment at every time step:

$$\Delta D_{\exp(n,m)}(t) = \frac{D_{\exp(n,m)}(t) - D_{\mathrm{ctrl}(m)}(t)}{D_{\mathrm{ctrl}(m)}(t)} \times 100, \quad (1)$$

where n is experiment number (05, 06, 07 or 08), m is each model and t is the year. This approach reduced biases from intermodel feature differences.

Ensemble means were then calculated for each experiment (Extended Data Fig. 7):

$$\Delta D_{\exp(n)}(t) = \overline{\Delta D_{\exp(n,m)}(t)}. \quad (2)$$

Lastly, we grouped damage change projections at year 2100 by Representative Concentration Pathway (RCP) scenarios: exp.07 (RCP2.6) and exp.05, 06 and 08 (RCP8.5)[48]. Integrated values were computed per sector after masking grounded ice. Spatial and integrated projections are shown in Fig. 4 and Extended Data Figs. 8 and 9.

It is crucial to note that ISMIP-6 experiments were designed to explore the diverse responses of ice sheet models under RCP scenarios rather than representing a mean trajectory. Consequently, the resulting damage change projections should also be interpreted as a potential range (sensitivity and sign) rather than as a single forecast. Moreover, the random forest model computes instantaneous damage values at each time step, and hence the calculated damage changes do not account for advection or history of damage features.

Data availability

The RAMP mosaic is available at the Alaska Satellite Facility via https://asf.alaska.edu/data-sets/derived-data-sets/ramp/ramp-get-ramp-data/. Sentinel-1 orbits are publicly available, and were accessed through the Google Earth Engine (GEE), for which the code is included in the repository accompanying this manuscript at https://github.com/mizeboud/antarctic-damage-change (ref. 36). ITS_LIVE velocity composites[40] are available through the data portal at https://nsidc.org/apps/itslive/, the REMA mosaic[39] was accessed as GEE asset 'UMN/PGC/REMA/V1_1/8m'. Ice sheet model output data of models participating in the ISMIP-6 project are available through a Globus endpoint[49]; instructions and information are available at GHub https://theghub.org/groups/ismip6/wiki. The produced annual damage maps can be viewed in GEE via https://code.earthengine.google.com/1984c17a29c3720e7ad3327a79a81527, or downloaded as NetCDF/GeoTiff format at the 4TU research data repository via https://doi.org/10.4121/70f914ee-b20d-4682-b2ec-54eddcc8569d (ref. 50). Annual ice-front positions were obtained from https://github.com/chadagreene/ice-shelf-geometry (ref. 31), and intersected with the MEaSUREs grounding line[32], available at the National Snow and Ice Data Center (NSIDC) via https://nsidc.org/data/nsidc-0709/versions/2. The adjusted annual ice shelf polygons, and other supplementary data such as a list of all processed orbits of Sentinel-1, supporting shapefiles and NetCDF files of projected damage values, are available at the 4TU research data repository via https://doi.org/10.4121/911e8799-f0dc-42e3-82b4-766ad680a71e (ref. 51).

Code availability

The NeRD method is available at https://doi.org/10.5281/zenodo.16759609 (ref. 52). The code used in this work to pre- and post-process data, and to develop and apply the random forest model, is available at Zenodo via https://doi.org/10.5281/zenodo.16759664 (ref. 36).

References

34. Jezek, K. C., Sohn, H. G. & Noltimier, K. F. Radarsat Antarctic mapping project. In *International Geoscience and Remote Sensing Symposium (IGARSS)*, Vol. 5, 2462–2464 (1998).
35. Gorelick, N. et al. Google Earth Engine: planetary-scale geospatial analysis for everyone. *Remote Sens. Environ.* https://doi.org/10.1016/j.rse.2017.06.031 (2017).
36. Izeboud, M. mizeboud/antarctic-damage-change: supporting code (v.1.0). *Zenodo* https://doi.org/10.5281/zenodo.16759664 (2025).
37. Husman, S. D. R. et al. Remote sensing of surface melt on antarctica: opportunities and challenges. *IEEE J. Sel. Top. Appl. Earth Obs. Remote Sens.* **16**, 2462–2480 (2023).
38. Watkins, R. H., Bassis, J. N., Thouless, M. D. & Luckman, A. High basal melt rates and high strain rates lead to more fractured ice. *J. Geophys. Res. Earth Surf.* **129**, e2023JF007366 (2024).
39. Howat, I. M., Porter, C., Smith, B. E., Noh, M. J. & Morin, P. The reference elevation model of Antarctica. *Cryosphere* **13**, 665–674 (2019).
40. Gardner, A. S., Fahnestock, M. A. & Scambos, T. A. MEaSUREs ITS_LIVE Landsat image-pair glacier and ice sheet surface velocities (NSIDC-0775, Version 1). *NASA National Snow and Ice Data Center Distributed Active Archive Center*. https://nsidc.org/data/nsidc-0775/versions/1 (2019).
41. Alley, K. E. et al. Continent-wide estimates of Antarctic strain rates from Landsat 8-derived velocity grids. *J. Glaciol.* **54**, 321–332 (2018).
42. Banwell, A. F. et al. Calving and rifting on the McMurdo Ice Shelf, Antarctica. *Ann. Glaciol.* **58**, 78–87 (2017).

43. Nawar, S. & Mouazen, A. Comparison between random forests, artificial neural networks and gradient boosted machines methods of on-line vis–NIR spectroscopy measurements of soil total nitrogen and total carbon. *Sensors* **17**, 2428 (2017).
44. Ahmad, M. W., Mourshed, M. & Rezgui, Y. Trees vs neurons: comparison between random forest and ANN for high-resolution prediction of building energy consumption. *Energy Build.* **147**, 77–89 (2017).
45. Han, T., Jiang, D., Zhao, Q., Wang, L. & Yin, K. Comparison of random forest, artificial neural networks and support vector machine for intelligent diagnosis of rotating machinery. *Trans. Inst. Meas. Control* **40**, 2681–2693 (2018).
46. Ploton, P. et al. Spatial validation reveals poor predictive performance of large-scale ecological mapping models. *Nat. Commun.* **11**, 4540 (2020).
47. Roberts, D. R. et al. Cross-validation strategies for data with temporal, spatial, hierarchical, or phylogenetic structure. *Ecography* **40**, 913–929 (2017).
48. Nowicki, S. et al. Experimental protocol for sea level projections from ISMIP6 stand-alone ice sheet models. *Tore Hattermann* https://doi.org/10.5194/tc-14-2331-2020 (2020).
49. Nowicki, S., Simon, E. & ISMIP6 Team. ISMIP6 21st century Antarctic projections https://theghub.org/groups/ismip6/wiki (2021).
50. Nye, J. F. A method of determining the strain-rate tensor at the surface of a glacier. *J. Glaciol.* **3**, 409–419 (1959).
51. Izeboud, M., Lhermitte, S., de Roda Husman, S. & Wouters, B. Annual damage maps of Antarctic ice shelves. 4TU.ResearchData Version 1 https://doi.org/10.4121/70f914ee-b20d-4682-b2ec-54eddcc8569d.v1 (2025).
52. Izeboud, M., Lhermitte, S., Wouters, B. & de Roda Husman, S. Supporting data for 'Damage development on Antarctic ice shelves sensitive to climate warming'. 4TU.ResearchData Version 1 https://doi.org/10.4121/911e8799-f0dc-42e3-82b4-766ad680a71e.v1 (2025).
53. Izeboud, M. mizeboud/NormalisedRadonTransform: NeRD algorithm (v.1.0). *Zenodo* https://doi.org/10.5281/zenodo.16759609 (2025).

Acknowledgements

M.I. and S.R.H. were funded by the Dutch Research Council (NWO) under grant numbers ALWGO.2018.043 and OCENW.GROOT.2019.091, respectively.

Author contributions

M.I. and S.L. conceived and designed the study. M.I. carried out the data processing, applied the detection method, developed the RF model and performed the analysis. S.R.H. provided guidance on the development of the random forest model and B.W. contributed to ice sheet model data analysis. All authors actively participated in scientific discussions, and contributed to the analysis and interpretation of the results. M.I. wrote the manuscript with contributions from all coauthors.

Competing interests

The authors declare no competing interests.

Additional information

Extended data is available for this paper at https://doi.org/10.1038/s41558-025-02453-4.

Correspondence and requests for materials should be addressed to Maaike Izeboud.

Peer review information *Nature Climate Change* thanks the anonymous reviewers for their contribution to the peer review of this work.

https://doi.org/10.1038/s41558-025-02453-4

Extended Data Table 1 | Overview of features used in the Random Forest regression model

Name	Description	Unit	RF feature importance	(Derived from) Observational Dataset		(Derived from) ISMIP-6 parameter	Function
				Source	Observation period	Parameter name	
Surface elevation	Used as proxy for ice thickness	m	0.195	REMA	constant	orog	-
Longitudinal strain rate	Strain-rate tensor component, parallel to the local flow direction	1/yr	0.148	ITS_LIVE vx, vy	Annual, 2015–2021	xvelsurf, yvelsurf	$\dot{\epsilon}_{lon} = \dot{\epsilon}_x \cos^2(\alpha) + 2\dot{\epsilon}_{xy} \cos(\alpha) \sin(\alpha) + \dot{\epsilon}_y \sin^2(\alpha)$
Ice flow velocity	Local ice flow speed	m/yr	0.146	ITS_LIVE vx, vy	Annual, 2015–2021	xvelsurf, yvelsurf	$v = \sqrt{v_x^2 + v_y^2}$
Effective strain rate	Measure of total strain rate, combining strain rate tensor components	1/yr	0.115	ITS_LIVE vx, vy		xvelsurf, yvelsurf	$\dot{\epsilon}_{eff} = \sqrt{\dot{\epsilon}_x^2 + \dot{\epsilon}_y^2 + \dot{\epsilon}_{xy}^2 + \dot{\epsilon}_x \dot{\epsilon}_y}$
Max principal strain rate (ε_1)	Principal component of the strain-rate tensor, oriented along the axis of greatest extension	1/yr	0.102	ITS_LIVE vx, vy	Annual, 2015–2021	xvelsurf, yvelsurf	$\dot{\epsilon}_1 = \frac{\dot{\epsilon}_x + \dot{\epsilon}_y}{2} + \sqrt{\left(\frac{\dot{\epsilon}_x - \dot{\epsilon}_y}{2}\right)^2 + \dot{\epsilon}_{xy}^2}$
Velocity change	Annual change of ice flow velocity magnitude	m/yr^2	0.084	ITS_LIVE vx, vy	Annual, 2015–2021	xvelsurf, yvelsurf	$\Delta v = v(t = y_2) - v(t = y_1)$, smoothed with a 3-year trailing mean
Strain-rate change	Annual change of max principal strain rate	1/yr^2	0.080	ITS_LIVE vx, vy	Annual, 2015–2021	xvelsurf, yvelsurf	$\Delta \dot{\epsilon} = \dot{\epsilon}_1(y_2) - \dot{\epsilon}_1(y_1)$, smoothed with a 3-year trailing mean
Transverse strain rate	Strain-rate tensor component, perpendicular to the local flow direction	1/yr	0.070	ITS_LIVE vx, vy	Annual, 2015–2021	xvelsurf, yvelsurf	$\dot{\epsilon}_{trans} = \dot{\epsilon}_x \sin^2(\alpha) - 2\dot{\epsilon}_{xy} \cos(\alpha) \sin(\alpha) + \dot{\epsilon}_y \cos^2(\alpha)$
Shear strain rate	Strain-rate tensor component	1/yr	0.060	ITS_LIVE vx, vy	Annual, 2015–2021	xvelsurf, yvelsurf	$\dot{\epsilon}_{shear} = (\dot{\epsilon}_y - \dot{\epsilon}_x) \cos(\alpha) \sin(\alpha) + \dot{\epsilon}_{xy} \left(\cos^2(\alpha) - \sin^2(\alpha)\right)$
Min principal strain rate (ε_2)	Principal component of the strain rate tensor, oriented along the axis of greatest shortening	1/yr	n/a	ITS_LIVE vx, vy	Annual, 2015–2021	xvelsurf, yvelsurf	$\dot{\epsilon}_2 = \frac{\dot{\epsilon}_x + \dot{\epsilon}_y}{2} + \sqrt{\left(\frac{\dot{\epsilon}_x - \dot{\epsilon}_y}{2}\right)^2 + \dot{\epsilon}_{xy}^2}$
Strain rate tensor	Two-dimensional strain rate tensor	1/yr	n/a	Nye, 1959 [48]			$\dot{\epsilon} = \begin{bmatrix} \frac{\partial u}{\partial x} & \frac{1}{2}\left(\frac{\partial v}{\partial x} + \frac{\partial u}{\partial y}\right) \\ \frac{1}{2}\left(\frac{\partial v}{\partial x} + \frac{\partial u}{\partial y}\right) & \frac{\partial v}{\partial y} \end{bmatrix} = \begin{bmatrix} \dot{\epsilon}_x & \dot{\epsilon}_{xy} \\ \dot{\epsilon}_{xy} & \dot{\epsilon}_y \end{bmatrix}$

Features are sorted for relative feature importance (most important at top), which total to 1. α is the flow angle, defined counter-clockwise from x-axis. The strain rate tensor is included to provide detail on the used functions[41,53].

https://doi.org/10.1038/s41558-025-02453-4

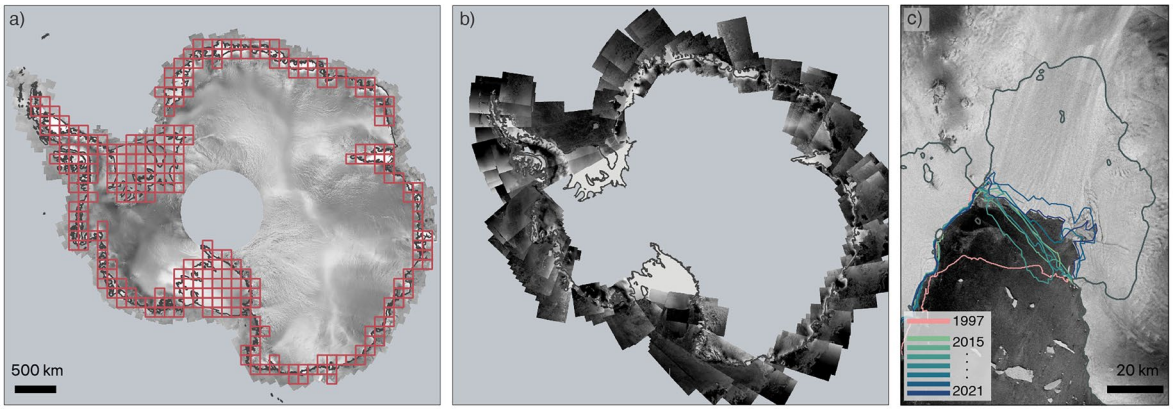

Extended Data Fig. 1 | Overview of used datasets to produce damage assessments. (**a**) RAMP mosaic from 1997[34], processed with NeRD only for data within the red tiles that cover all ice shelves. (**b**) Data coverage of Sentinel-1 EW ascending orbit images in one assessment year (2021), showing data gaps on the Filchner–Ronne, Ross and Amery Ice Shelves. (**c**) Example of annual calving front positions at the Pine Island Glacier, adapted from Greene et al.[31] with manual corrections to fit the used Sentinel-1 images. Grounding line from[32] in black. Grounding line shapefiles in **a**–**c** from ref. 32 under a Creative Commons licence CC BY. Ice-front shapefile in **c** from ref. 31 under a Creative Commons license CC BY.

https://doi.org/10.1038/s41558-025-02453-4

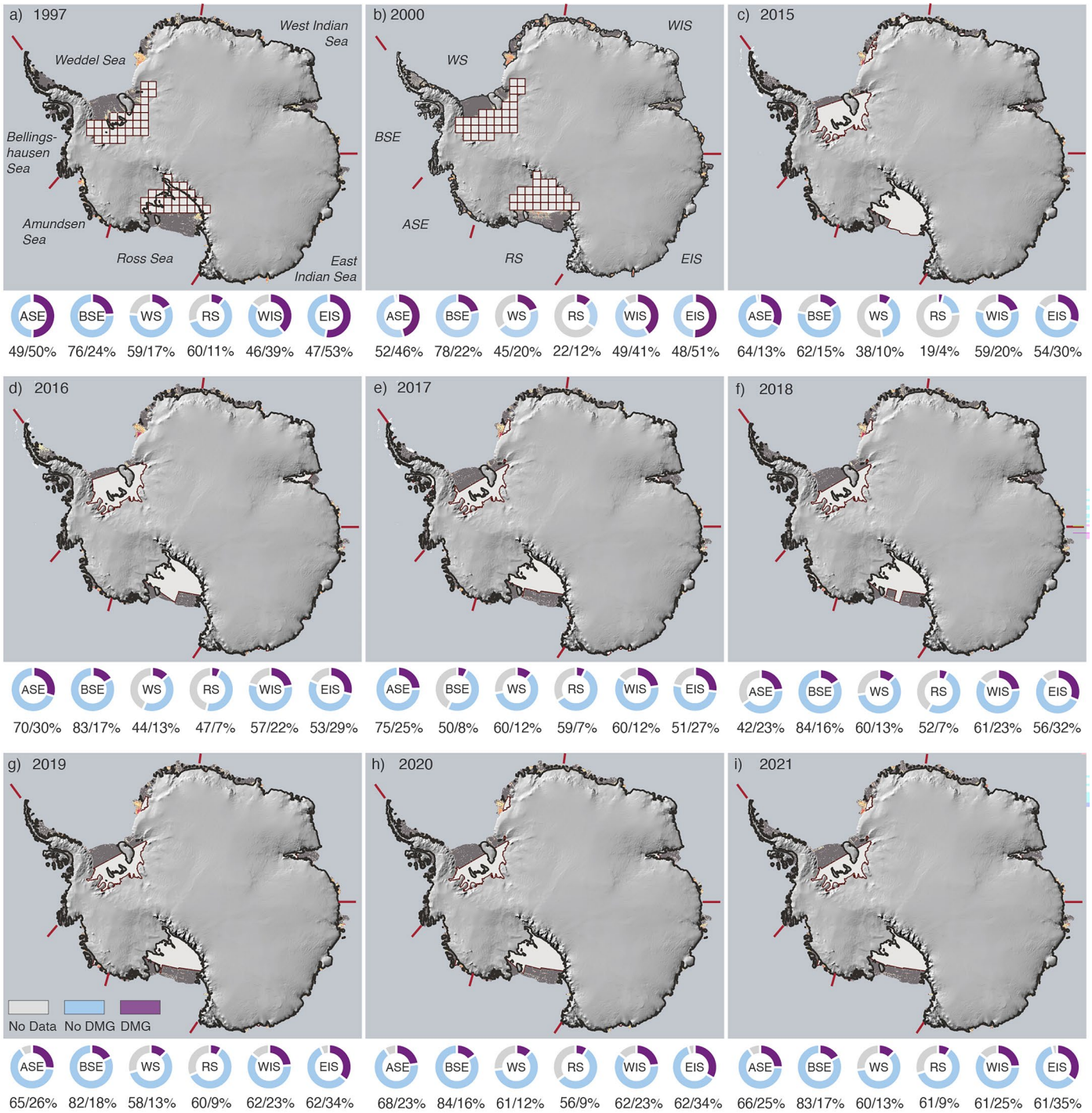

Extended Data Fig. 2 | Annual damage assessments obtained from NeRD algorithm. Panels **a, b** show damage maps for 1997, 2000 respectively and **c-i** show every year from 2015 to 2021. No-data areas are shown in grey; red tiles in the 1997 and 2000 RAMP mosaic were excluded to match Sentinel-1 Coverage (2015–2021). The pie charts show aggregated sector values by pixel count: no-data (light grey), no-damage (light blue, $\hat{D} = 0$) and damaged (purple, $\hat{D} > 0$). Percentages are provided for the no-damage and damaged class. The total ice shelf area varies per year based on annual calving front positions. Grounded ice[32] is visualized with Antarctic DEM[33]. Basemaps in **a**–**i** from ref. 33 under a Creative Commons licence CC BY. Grounding line shapefiles in **a**–**i** from ref. 32 under a Creative Commons licence CC BY.

https://doi.org/10.1038/s41558-025-02453-4

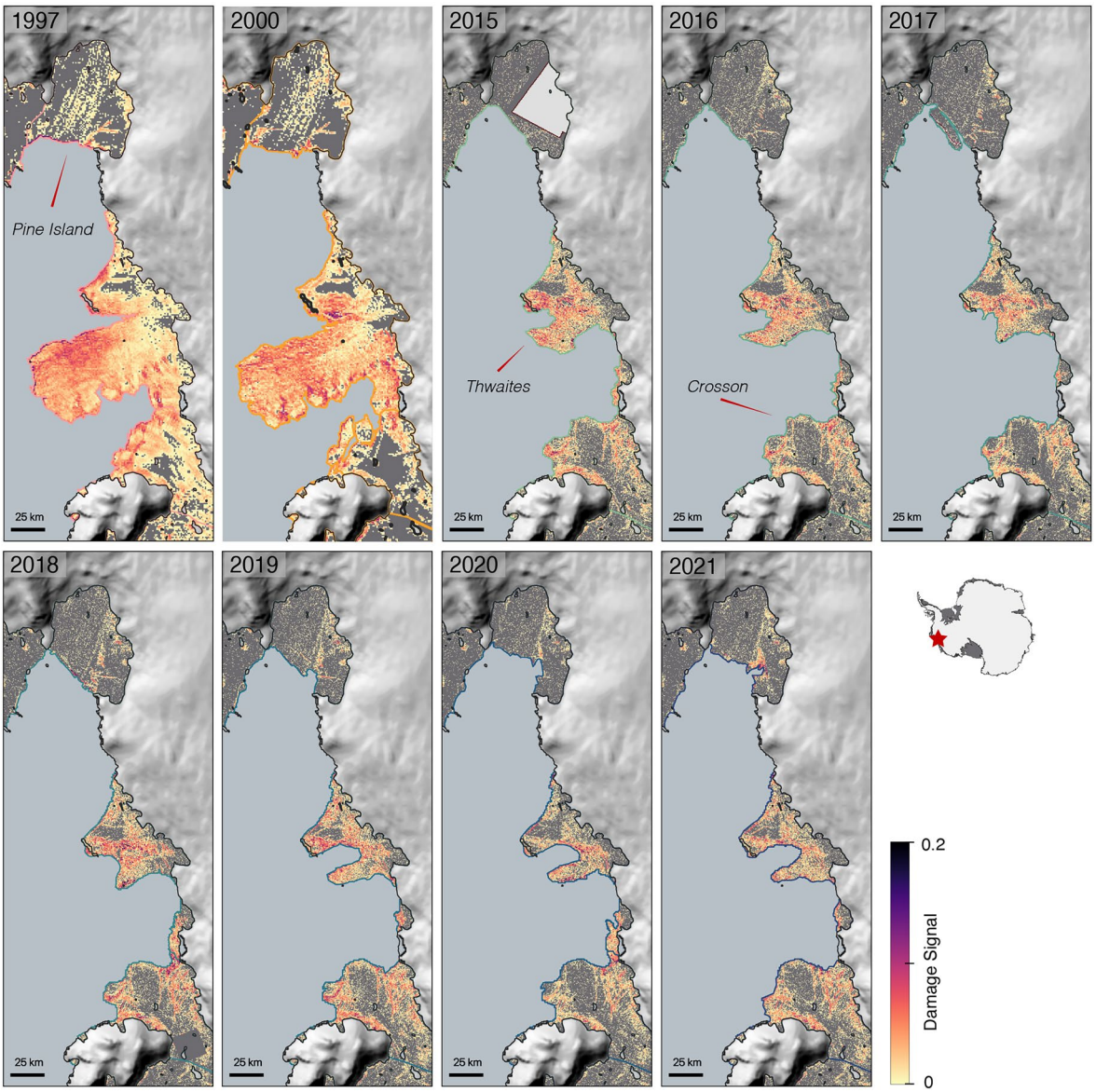

Extended Data Fig. 3 | Damage maps of ice shelves in Amundsen Sea Embayment for assessed years. Detected damage by NeRD on RAMP AMM and MAMM mosaics (1997, 2000) at 1000 m spatial resolution, and Sentinel-1 SAR imagery obtained in September-Oktober-November each year between 2015–2021 at 400 m resolution. Data is clipped to annual ice shelf front positions and static grounding line[31,32]; background is shaded Antarctic DEM[33]. Uniform grey areas indicate no-data coverage for that year. Basemaps in **a**–**i** from ref. 33 under a Creative Commons licence CC BY. Grounding line shapefiles in **a**–**i** from ref. 32 under a Creative Commons licence CC BY. Ice-front shapefiles in **a**–**i** from ref. 31 under a Creative Commons license CC BY.

https://doi.org/10.1038/s41558-025-02453-4

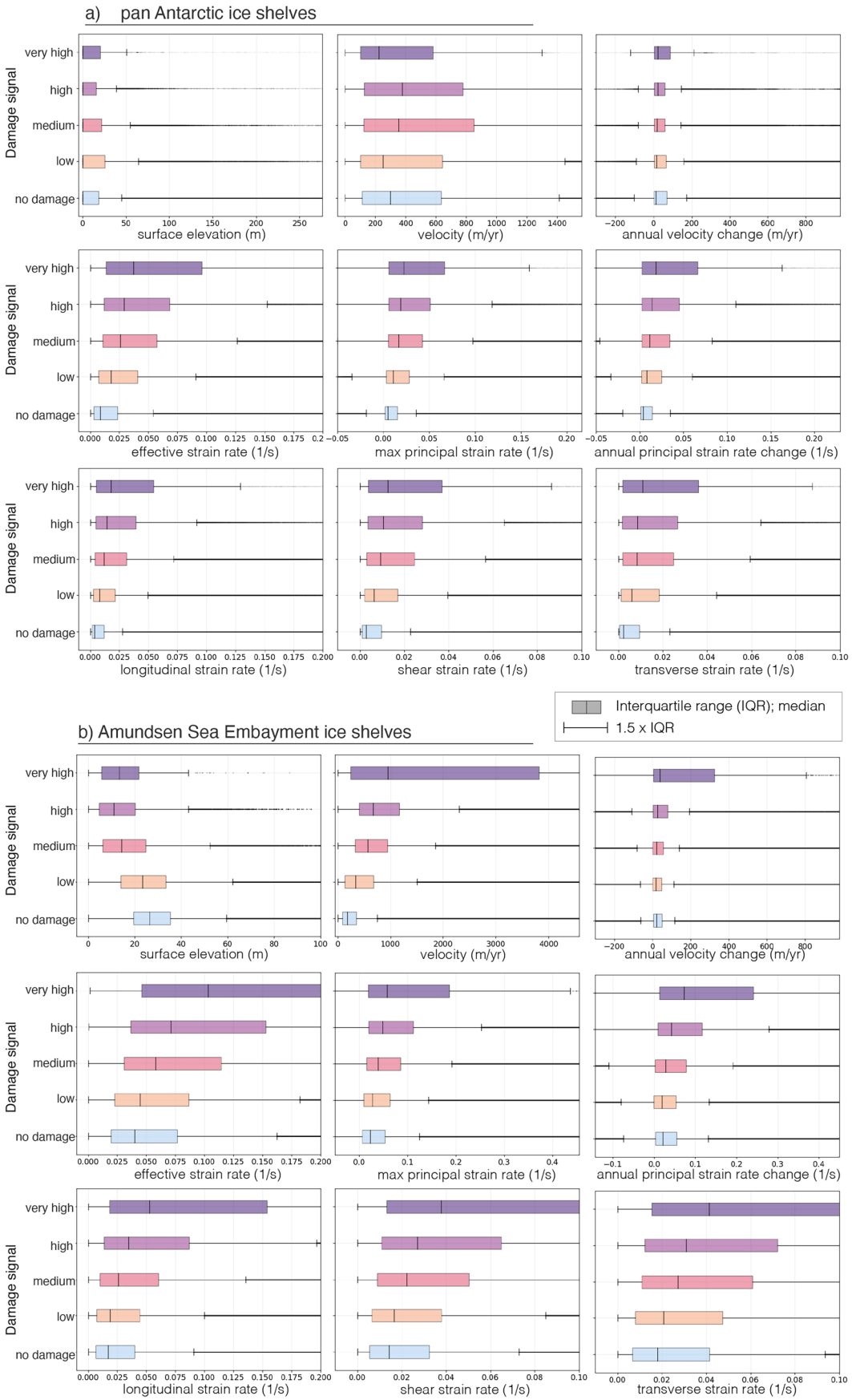

Extended Data Fig. 4 | See next page for caption.

https://doi.org/10.1038/s41558-025-02453-4

Extended Data Fig. 4 | Random Forest input feature information. Box-plot of input features used for training the RF model on (**a**) pan-Antarctic scale and (**b**) in the Amundsen Sea Embayments. showing interquantile range. Damage signal values are binned by low to high signal values, to favour visualization of the minority (high damage signal) class (low: $\hat{D} \in (0,0.0125]$, medium: $\hat{D} \in (0.0125,0.0625]$, high: $\hat{D} \in (0.0625,0.1625]$ and very high: $\hat{D} \in (0.1625,0.5]$). Boxes show inter-quartile range (IQR, Q1-Q3) and whiskers extend from the box to the farthest data point lying within 1.5x the IQR.

https://doi.org/10.1038/s41558-025-02453-4

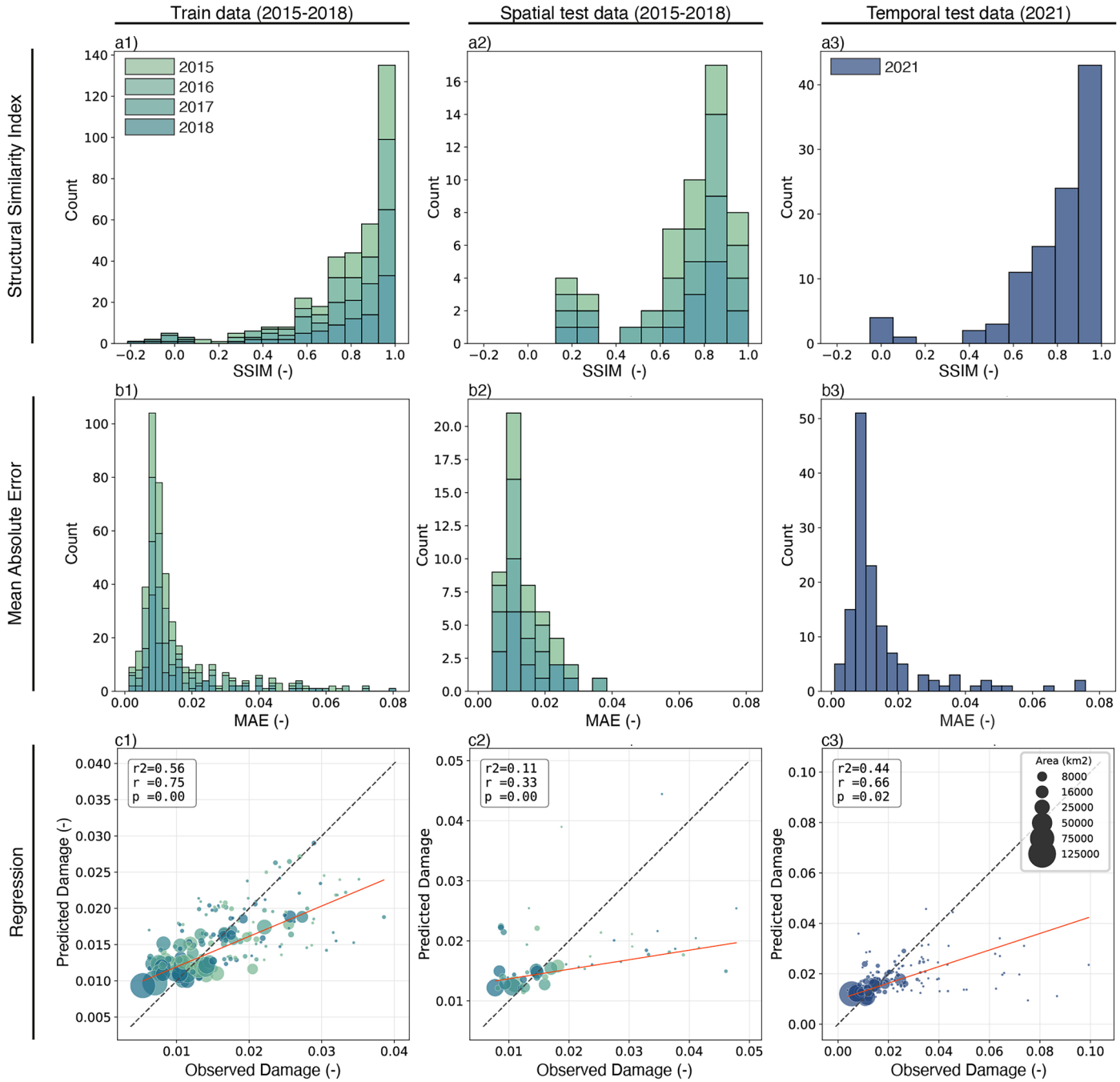

Extended Data Fig. 5 | Evaluation of the Random Forest regression model. Performance for training (a1-c1) and testing dataset, split in the spatial test set (a2-c2) and temporal test set (a3-c3). a1-a3 show the Structural Similarity Index calculated for each ice shelf, b1-b3 the Mean Absolute Error calculated for each ice shelf, and c1-c3 the regression of observed versus predicted values, weighted for the area of each ice shelf.

https://doi.org/10.1038/s41558-025-02453-4

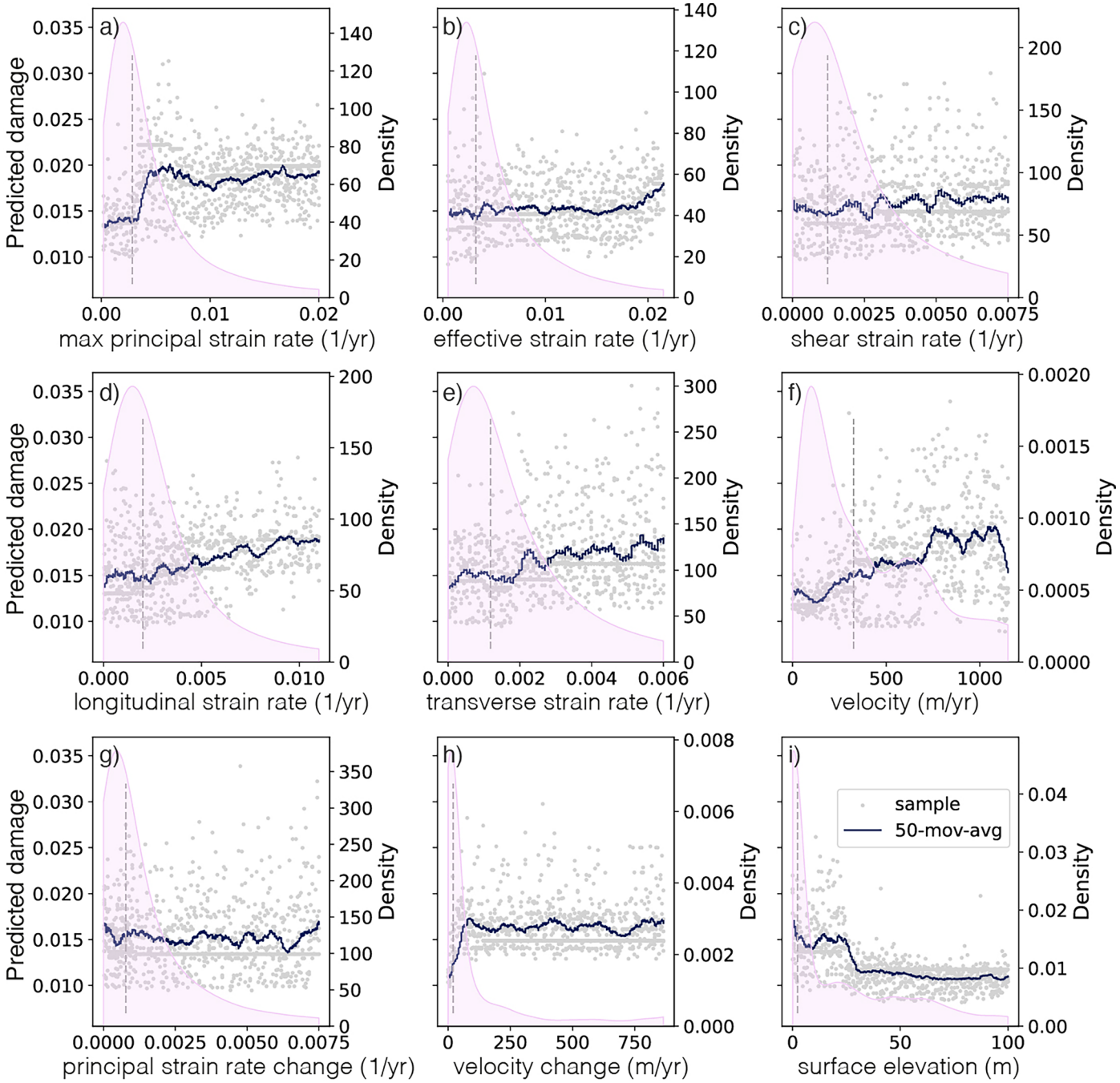

Extended Data Fig. 6 | Random Forest prediction related to input parameters. Panels for (**a**) maximum principal strain rate, (**b**) effective strain rate, (**c**) shear strain rate, (**d**) longitudinal strain rate, (**e**) transverse strain rate, (**f**) velocity, (**g**) principal strain rate change, (**h**) velocity change, (**i**) surface elevation. Each panel shows damage predictions made with the RF model, varying one parameter at a time from their 5 to 95 percentile value within the training dataset. All other parameters were set to their median value within the training dataset, adding small random Gaussian noise perturbations (< 5% of respective standard deviation). Each correlation plot is made with 750 samples (grey dots). A moving average of 50 samples is plotted in blue. Shaded in pink are the data distributions of each parameter within the training dataset and their median in dashed grey line.

https://doi.org/10.1038/s41558-025-02453-4

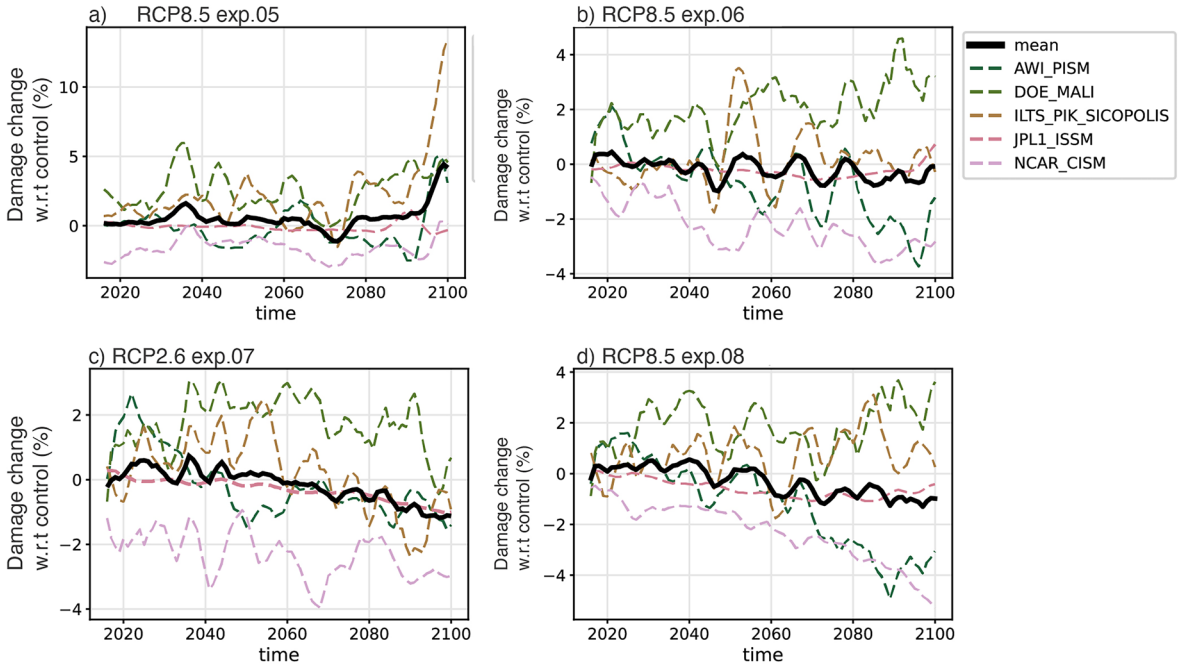

Extended Data Fig. 7 | Model ensembles of predicted damage change between 2015-2100. Shown for each climate forcing experiment, experiment 05 (**a**), 06 (**b**), 07 (**c**) and experiment 08 (**d**). Each panel shows predicted values of damage change (%) with respect to the control simulation of each model, with the ensemble mean in black, smoothed with a 5-year running mean.

https://doi.org/10.1038/s41558-025-02453-4

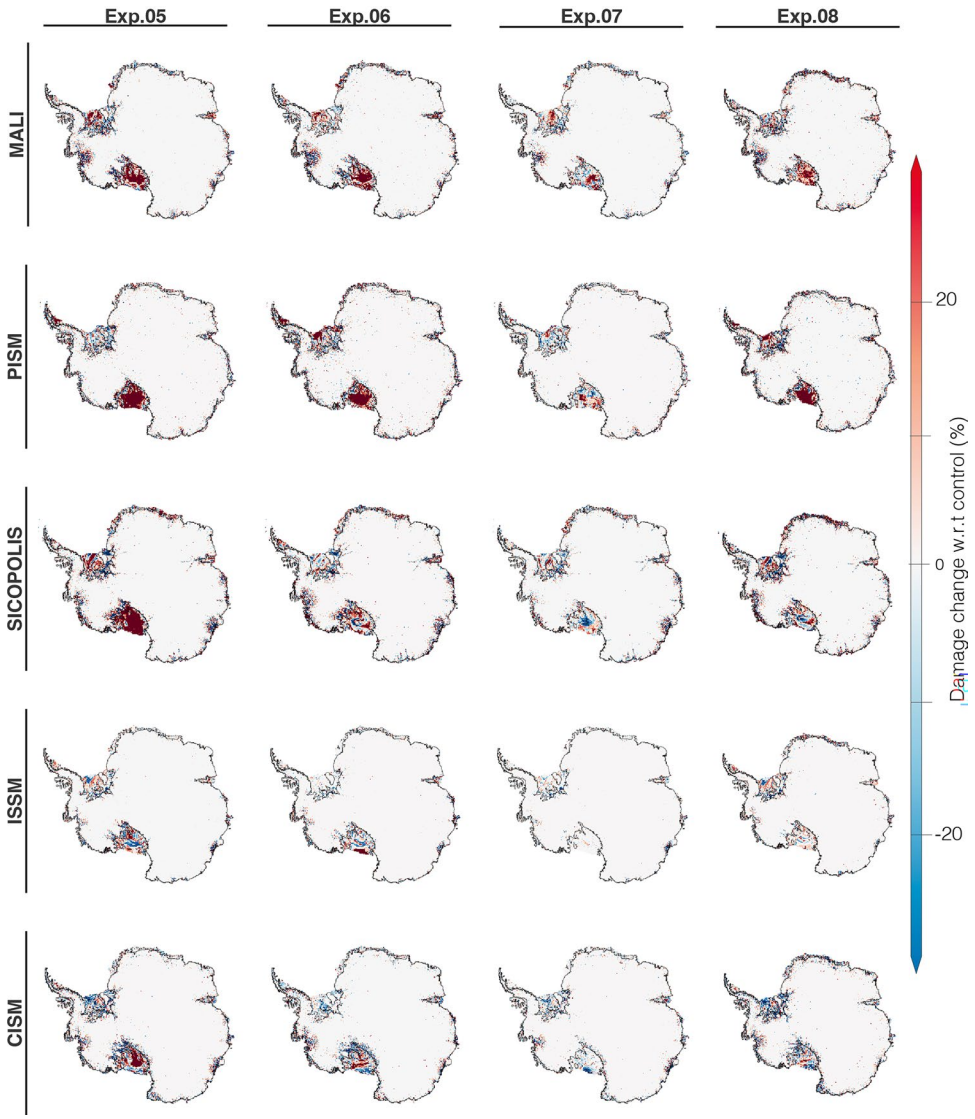

Extended Data Fig. 8 | Spatial plots of predicted damage change (%) at year 2100. Damage change is calculated with respect to the control simulation, shown for each climate forcing experiment and ice sheet model. Grounding line added in black[32]. Grounding line shapefiles from ref. 32 under a Creative Commons licence CC BY.

https://doi.org/10.1038/s41558-025-02453-4

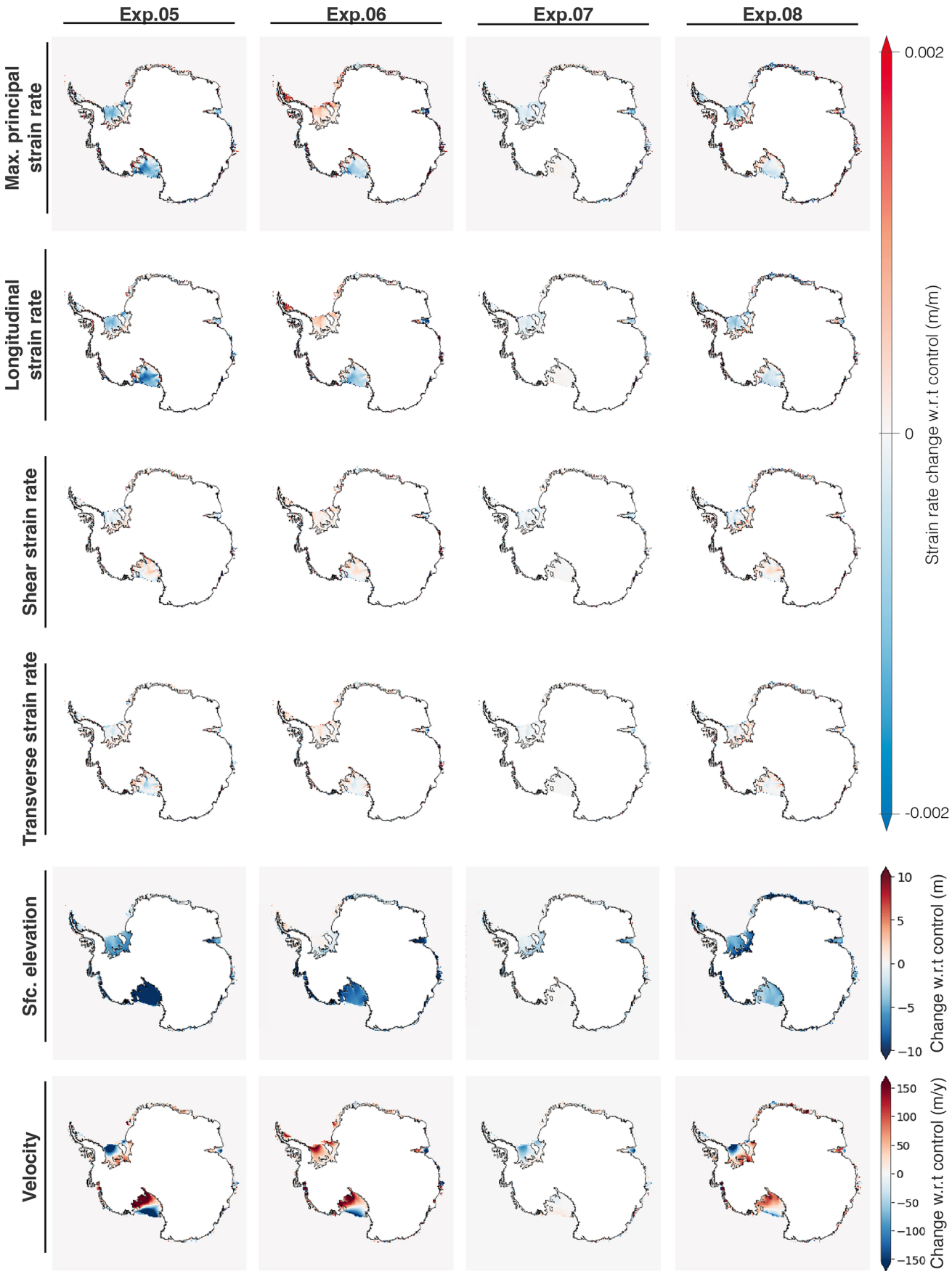

Extended Data Fig. 9 | Spatial plots of projected change of ice parameters at year 2100. Panels show the parameters used as input to generate damage prediction, obtained from ISMIP-6 model data. Shown are model ensemble means of absolute change values of each parameter for the selected experiment with respect to the control simulation. Grounding line added in black[32]. Grounding line shapefiles from ref. 32 under a Creative Commons licence CC BY.